THE LOCAL GROUP IN THE COSMIC WEB

J. E. Forero-Romero[1] and R. González[2,3]

[1] Departamento de Física, Universidad de los Andes, Cra. 1 No. 18A-10, Edificio Ip, Bogotá, Colombia
[2] Instituto de Astrofísica, Pontificia Universidad Católica de Chile, Av. Vicuña Mackenna 4860, Santiago, Chile
[3] Centro de Astro-Ingeniería, Pontificia Universidad Católica de Chile, Av. Vicuña Mackenna 4860, Santiago, Chile

ABSTRACT

We explore the characteristics of the cosmic web around Local Group(LG) like pairs using a cosmological simulation in the ΛCDM cosmology. We use the Hessian of the gravitational potential to classify regions on scales of ~ 2 Mpc as a peak, sheet, filament or void. The sample of LG counterparts is represented by two samples of halo pairs. The first is a general sample composed by pairs with similar masses and isolation criteria as observed for the LG. The second is a subset with additional observed kinematic constraints such as relative pair velocity and separation. We find that the pairs in the LG sample with all constraints are: (i) Preferentially located in filaments and sheets, (ii) Located in in a narrow range of local overdensity $0 < \delta < 2$, web ellipticity $0.1 < e < 1.0$ and prolateness $-0.4 < p < 0.4$. (iii) Strongly aligned with the cosmic web. The alignments are such that he pair orbital angular momentum tends to be perpendicular to the smallest tidal eigenvector, $\hat{e}_3$, which lies along the filament direction or the sheet plane. A stronger alignment is present for the vector linking the two halos with the vector $\hat{e}_3$. Additionally, we fail to find a strong correlation of the spin of each halo in the pair with the cosmic web. All these trends are expected to a great extent from the selection on the LG total mass on the general sample. Applied to the observed LG, there is a potential conflict between the alignments of the different planes of satellites and the numerical evidence for satellite accretion along filaments; the direction defined by $\hat{e}_3$. This highlights the relevance of achieving a precise characterization of the place of the LG in the cosmic web in the cosmological context provided by ΛCDM.

Subject headings: galaxies: Local Group — dark matter

1. INTRODUCTION

The spatial and kinematic configuration of the Local Group (LG) galaxies is very uncommon in the local Universe and in cosmological simulations. The LG is dominated by two big spirals: the Milky Way (MW) and M31, the next most-luminous galaxy is M33 which is ~ 10 times less massive than M31, followed by several dozen less luminous dwarf galaxies, up to a distance of ~ 3Mpc. The velocity vector of M31, with a low tangential velocity is consistent with a head-on collision orbit toward the MW (Cox & Loeb 2008; van der Marel et al. 2012b; Sohn et al. 2012).

Another feature of the Local Group is the relatively low velocity dispersion of nearby galaxies up to ~ 8 Mpc (Sandage & Tammann 1975; Aragon-Calvo et al. 2011, and references therein). The environment around the Local Group has density quite close to the average density of the universe (Klypin et al. 2003; Karachentsev 2005). In addition, the closest massive galaxy cluster, the Virgo Cluster, is ~ 16.5 Mpc away (Mei et al. 2007).

In addition, the LG is located in a diffuse and warped filament/wall connecting Virgo Cluster with Fornax Cluster, some nearby galaxies and groups members of this large structure are the Maffei group, NGC 6744, NGC 5128, M101, M81, NGC1023, Cen A group (Courtois et al. 2013). At this scale, there is no evident alignment of the MW-M31 orbital plane with any local filament or the Virgo-Fornax direction. However, if we look

je.forero@uniandes.edu.co
regonzar@astro.puc.cl

in a smaller volume below scales of ~ 6 Mpc, there is a clear alignment of the MW-M31 orbit with a local plane of galaxies as shown by Figure 3 in Courtois et al. (2013). On top of that, the satellite galaxies in the MW and M31 present different kinds of strong alignments along planes (Pawlowski et al. 2013; Shaya & Tully 2013), which are sometimes considered as unusual in the context of the Λ Cold Dark Matter (CDM) model (Pawlowski et al. 2012).

This combination of features makes LG analogues uncommon. Using numerical simulations González et al. (2014) found less than 2% MW-sized halos reside in a pair similar to MW-M31 and in a similar environment. Furthermore, if we select pairs constrained within 2σ error from current observational measurements of the velocity components and distance to M31, there are only 46 systems in a cubic volume of 250 h^{-1}Mpc side, giving a number density $\sim 1.0 \times 10^{-6}$Mpc^3, comparable to the abundance of massive clusters. A similar abundance was found by Forero-Romero et al. (2011) by comparing the formation history of LG pairs in constrained simulations with the results of unconstrained cosmological simulations.

Forero-Romero et al. (2013) also studied MW-M31 pairs in numerical simulations finding the typical quantities characterizing the orbital parameters of the LG are rare among typical pairs, but not sufficiently rare to challenge the ΛCDM model. Another set of criteria for LG analogues was used by Li & White (2008), but despite differences in the definitions and resulting fraction of LG analogues, results are in agreement with a low pairs frequency as well.

To better understand the properties of the LG and how this uncommon pair configuration can be explained in the cosmological context, some questions arise. What else can we say of the environment of the LG on larger scales? To what extent is this an expected configuration in ΛCDM? In particular, which are the typical/preferred locations of these systems within the Cosmic Web? Are the preferential alignments of satellites a result of the location of the LG in the Cosmic Web?

In this paper we address those questions by studying the large scale environment of LG analogues in the context of ΛCDM . We use the Bolshoi simulation to explore in what structures they reside and if there is any correlation or alignment with the cosmic web. The large scale environment is defined by the cosmic web components identified by Forero-Romero et al. (2009), and we use the LG analogues computed by González et al. (2014).

This paper is organized as follows. In Section 2 we present the N-body cosmological simulation and the algorithm to define the cosmic web, next in Section 3 we describe the sample of LG analogues extracted from the simulation. In Section 4 we present our results to wrap up with a discussion and conclusions in Section 5.

2. SIMULATION AND WEB FINDING ALGORITHM

2.1. *The Bolshoi simulation*

We use the Bolshoi simulation of ΛCDM cosmology: $\Omega_{\rm m} = 1 - \Omega_\Lambda = 0.27$, $H_0 = 70\,{\rm km/s/Mpc}$, $\sigma_8 = 0.82$, $n_s = 0.95$ (Klypin et al. 2011), compatible with the constraints from the WMAP satellite (Hinshaw et al. 2013). The simulation followed the evolution of dark matter in a $250h^{-1}{\rm Mpc}$ box with spatial resolution of $\sim 1h^{-1}$ kpc and mass resolution of $m_{\rm p} = 1.35 \times 10^8$ M$_\odot$. Halos are identified with the BDM algorithm (Klypin & Holtzman 1997). The BDM algorithm is a spherical overdensity halo finding algorithm and is designed to identify both host halos and subhalos.

2.2. *Cosmic web identification*

The web finding algorithm is based on the tidal tensor computed as the Hessian of the gravitational potential field

$$T_{ij} = \frac{\partial^2 \phi}{\partial r_i \partial r_j}, \qquad (1)$$

where r_i, $i = 1, 2, 3$ refers to the three spatial comoving coordinates and ϕ is the gravitational potential renormalized to follow the Poisson equation $\nabla^2 \phi = \delta$ where δ is the matter overdensity.

This tensor is real and symmetric, which means that it can be diagonalized. We denote its eigenvalues as $\lambda_1 \geq \lambda_2 \geq \lambda_3$ and their corresponding eigenvectors $\hat{e}_1$, $\hat{e}_2$ and $\hat{e}_3$. The web classification compares each one of the three eigenvalues to a threshold value $\lambda_{\rm th}$. If the three, two, one or zero eigenvalues are larger than this threshold the region is classified as peak, filament, sheet or void, respectively. Because this tensor is also known as the tidal tensor we refer to it as the Tweb algorithm.

Forero-Romero et al. (2009) performed a detailed study for the topology of the cosmic web and its visual counterpart as a function of the parameter $\lambda_{\rm th}$. They found that reasonable results in terms of the volume fraction occupied by voids, the visual inspection and the halo populations in each web type can be reached by values of $0.2 < \lambda_{\rm th} < 0.4$. In this paper we choose the value of $\lambda_{\rm th} = 0.3$ to proceed with our analysis. This is only relevant to the classification of the simulation into web elements. Other results are completely independent of this choice. Nevertheless we have checked that the main conclusions of this work do not depend on the precise choice of $\lambda_{\rm th}$.

The algorithm to compute the potential is grid based. First we interpolate the mass into a cubic grid with a Cloud-In-Cell (CIC) scheme and smooth it with a Gaussian kernel in order to reduce the grid influence in the computations that follow. Then we obtain the gravitational potential using FFT methods and use finite differences to compute the Hessian at every point in the grid. In our case we have used a grid size and a Gaussian smoothing with two times larger as the typical separation between the two halos in the Local Group. The purpose of this choice is to have both halos in the pair a common environment. In this paper we use a grid spacing of $s = 0.97\,h^{-1}{\rm Mpc}$, corresponding to a 256^3 grid in the Bolshoi volume. The scale for the Gaussian smoothing uses the same value.

We use the matter overdensity, ellipticity and the prolatenes to further characterize the web. These quantities are defined in terms of the eigenvalues as follows

$$\delta = \lambda_1 + \lambda_2 + \lambda_3, \qquad (2)$$

$$e = \frac{\lambda_3 - \lambda_1}{2(\lambda_1 + \lambda_2 + \lambda_3)}, \qquad (3)$$

$$p = \frac{\lambda_1 + \lambda_3 - 2\lambda_2}{2(\lambda_1 + \lambda_2 + \lambda_3)}. \qquad (4)$$

We also measure the alignment of the LG halos with respect to the cosmic web defined by their eigenvectors. To this end we characterize each LG pair by two vectors. The first is $\hat{n}$, the axis along the orbital angular momentum of the pair, normal to its orbital plane; the second is $\hat{r}$, the vector that connects the halos in the pair which can be related to the alignment of the radial velocities to the web. We quantify the alignment using the absolute value of the cosine of the angle between the two vectors of interest $\mu = |\hat{e}_i \cdot \hat{n}|$ or $\mu = |\hat{e}_i \cdot \hat{r}|$, where $i = 1, 2, 3$.

We have veryfied that the main trends reported in this paper remain unchanged if we use the results from a 512^3 grid smoothed over scales of $s = 0.48h^{-1}{\rm Mpc}$. Small changes of a factor of ~ 2 in the smoothing scale do not significantly impact the cosmic web as it was shown in Forero-Romero et al. (2009) from the study of the volume and mass filling fractions for different smoothing scales. Other works have also shown that broad features the cosmic web, as defined in this paper, are robust to factor of ~ 2 changes on the scale defining the web (Cautun et al. 2014).

The data of the BDM halos and the Tweb is publicly available through a database located at http://www.cosmosim.org/. A detailed description of the database structure was presented by Riebe et al. (2013).
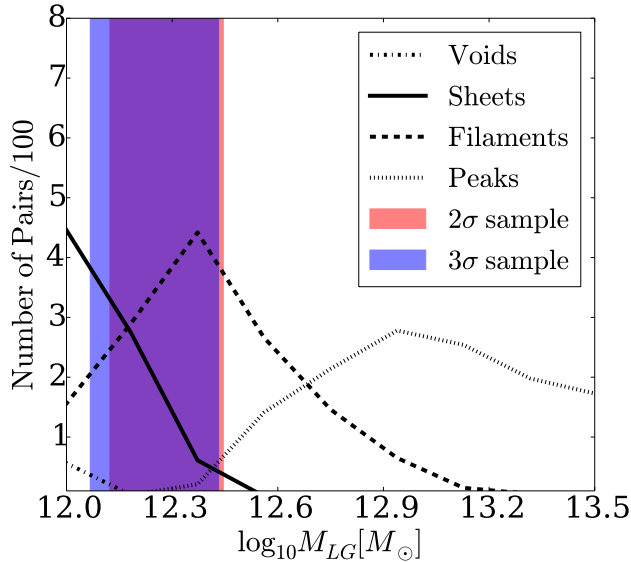
3. LOCAL GROUP ANALOGUES

FIG. 1.— Mass distribution of pairs in different environments for the general sample. The shaded regions show the 68% confidence interval of the mass ranges for 2σ and 3σ samples.

To construct a sample of the MW-M31 pairs at $z \sim 0$, we use a series of simulation snapshots at $z < 0.1$ (since the last ~ 1.3 Gyr) spaced by $\sim 150 - 250$ Myr. This is done because a particular configuration of MW and M31 is transient and corresponds to a relatively small number of systems at one snapshot. By using multiple snapshots we can increase the sample of systems in such configuration during a period of time in which secular cosmological evolution is small.

The LG analogues or the General Sample (GS) in this paper are pairs selected in relative isolation, and in a wide range of masses from $M_{200c} = 5 \times 10^{11}$ M$_\odot$ to 5×10^{13} M$_\odot$. Isolation criteria include pair members closer than 1.3Mpc, and with no massive neighbors within 5Mpc. In addition, we require that pairs have no Virgo-like neighbor halo with mass $M_{200c} > 1.5 \times 10^{14}$ M$_\odot$ within 12 Mpc. We have 5480 pairs under these general criteria. A full description of the selection criteria can be found in González et al. (2014, 2013).

We also define two subsets of restricted samples (RS) more closely related to the MW-M31 dynamics according to the tolerance in additional constraints. A sample named 2σ, corresponding to LG analogues constrained by two times the observational errors in the orbital values (radial velocity, tangential velocity, and separation), and a more relaxed sample named 3σ for LG analogues constrained by three times observational errors accordingly. The number of pairs in each sample is 46 and 120 respectively, notice we have less pairs than in González et al. (2014), since we removed pairs which are too close at $z = 0$, i.e. their virial radii overlap, also we removed a couple of pairs that merged or change their mass more than 20% at present time since they were detected at $z < 0.1$.

4. RESULTS

4.1. The preferred environment for LGs

The first result we explore is the kind of environment occupied by our LGs, and use as reference sample the GS where pairs are much more relaxed in mass and kinematic constraints. We find that the pairs in the GS are located across all different evironment without any strong preferences; 1/3 are located in sheets, 1/4 in peaks, 1/4 in filaments and the remaining 1/6 in voids.

The situation in the 2σ and 3σ samples is very different. By and large the LGs in these samples are located in filaments and sheets. In both samples, $\sim 50\%$ of the pairs can be found in filaments while $\sim 40\%$ are in sheets. These absolute numbers in each environment for each sample are presented in Table 1.

We find that the difference between the GS and the RS can be explained by the total pair mass. In González et al. (2014) the mass range covered by 2σ and 3σ samples is very narrow and it is used to constraint the LG mass. We show in Table 1 that a subset of the GS having a similar mass range than the RS reproduces similar environment fractions. The correlation between halo mass and their environment is a well known result (Lee & Shandarin 1998).

Figure 1 summarizes this correlation between environment an total pair mass. Each line represents the mass distribution of pairs in the four different environments for the GS. High mass pairs tend to be located in peaks and filaments while less massive ones in voids and sheets. The shaded regions represent the 68% confidence intervals of the mass distributions of 2σ and 3σ samples.

4.2. Web Overdensity, Ellipticity and Prolateness

We now characterize the preferred place of the pair samples in terms of the web overdensity, ellipticiy and anisotropy as defined in Section 2.

Figure 2 shows the dependency of these three characteristics on the total pair mass for the different samples. GS is represented by the solid lines with the associated errors covered by the shaded region. The symbols represents the results for the 2σ and 3σ samples. In the three cases it is evident that the range of values for the 2σ and 3σ samples are completely expected from the mass constraint alone.

The left panel shows the overdensity dependence on pair mass. Higher mass pairs are located in high density regions. The 2σ and 3σ samples having a narrower mass range as shown in previous figure, are consequently located within a narrower range of overdensities $0.0 < \delta < 2.0$ peaking at $\delta \sim 1$. This is also consistent with the fact that these samples are mostly found in filaments and sheets.

Middle and right panels show web ellipticity and absolute prolateness dependence on mass. Again we notice that within the 2σ and 3σ mass range, the average ellipticity and prolateness does not differ significantly from the GS expectation. In the RS samples the pairs are located in a narrow range for ellipticities $0.1 < e < 1.0$ and absolute prolateness $|p| < 0.4$.

4.3. Alignments with the cosmic web

We now study different alignments of the LG with respect to the cosmic web.

Orbital Angular Momentum. Figure 3 shows the cumulative distribution of $\mu \equiv \hat{e}_i \cdot \hat{n}$ for the three eigenvectors $i = 1, 2, 3$. Lines in each panel correspond to

Sample	Peak	Filament	Sheet	Void
	n (%)	n (%)	n (%)	n (%)
2σ	4 (8.7)	24 (52.2)	17 (36.7)	1 (2.2)
3σ	10 (8.3)	58 (48.3)	47 (39.2)	5 (4.2)
General	1312 (23.9)	1472 (26.9)	1769 (32.3)	927 (16.9)
General ($12.1 < \log_{10} M_{\mathrm{LG}}/\mathrm{M}_\odot < 12.3$)	8 (1.4)	334 (55.5)	259 (43.0)	1 (0.1)

TABLE 1

NUMBER OF PAIRS IN THE FOUR DIFFERENT KINDS OF ENVIRONMENTS FOR EACH OF THE THREE SAMPLES PRESENTED IN SECTION 3. IN PARENTHESIS THE SAME NUMBER AS A PERCENTAGE OF THE TOTAL POPULATION. THE LAST LINE IN THE TABLE CORRESPONDS TO THE GENERAL SAMPLE WITH AN ADDITIONAL MASS CUT FOR THE TOTAL PAIR MASS.
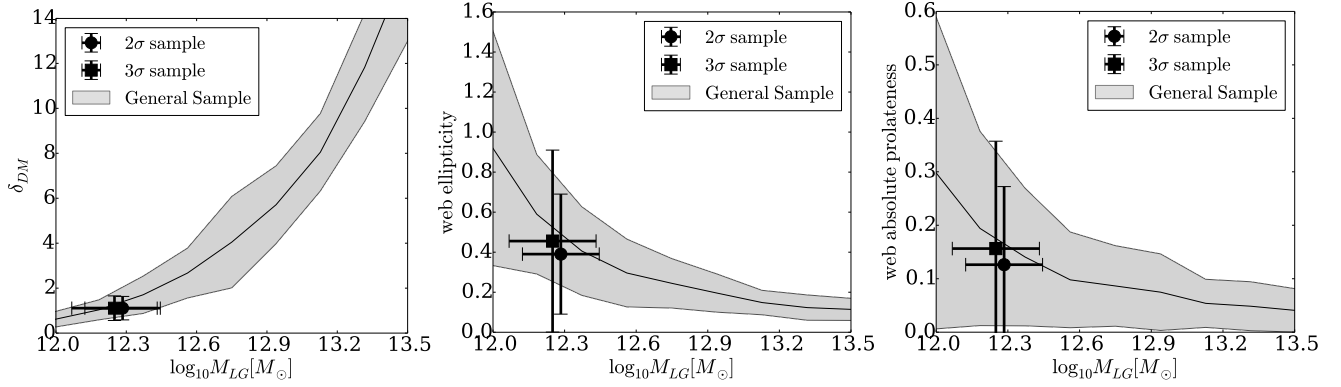
FIG. 2.— Mass dependency of the average dark matter overdensity (left), web ellipticity (middle) and web absolute value prolateness (right) at the pair location. The shaded contours indicate the 68% confidence region.
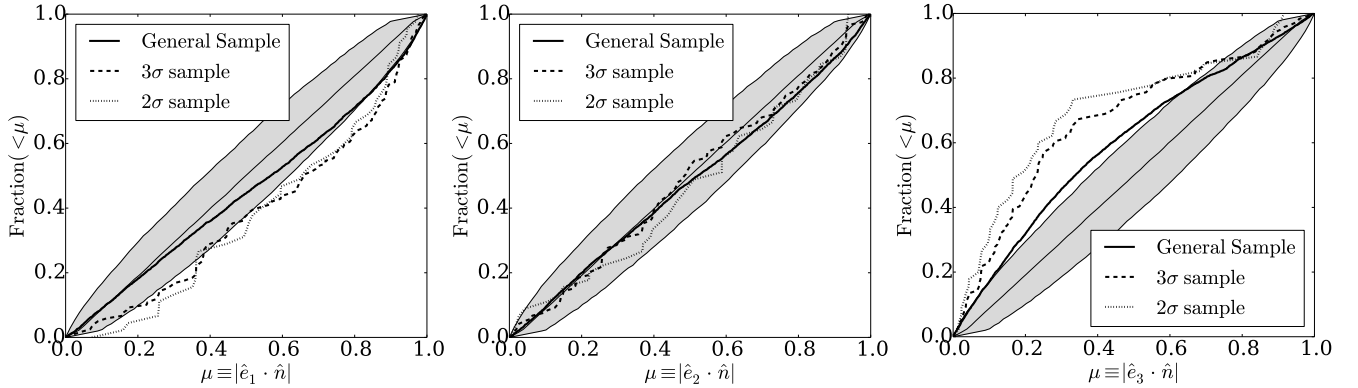

FIG. 3.— Cumulative distributions for the alignment between the normal vector to the pair orbital plane, $\hat{n}$, and the three eigenvectors in the Tweb. The shaded region shows the expectation for a random distribution without any preferential alignment, it encloses the 5% and 95% percentiles of 10000 flat distributions for μ generated with the same number of points as the 2σ sample.
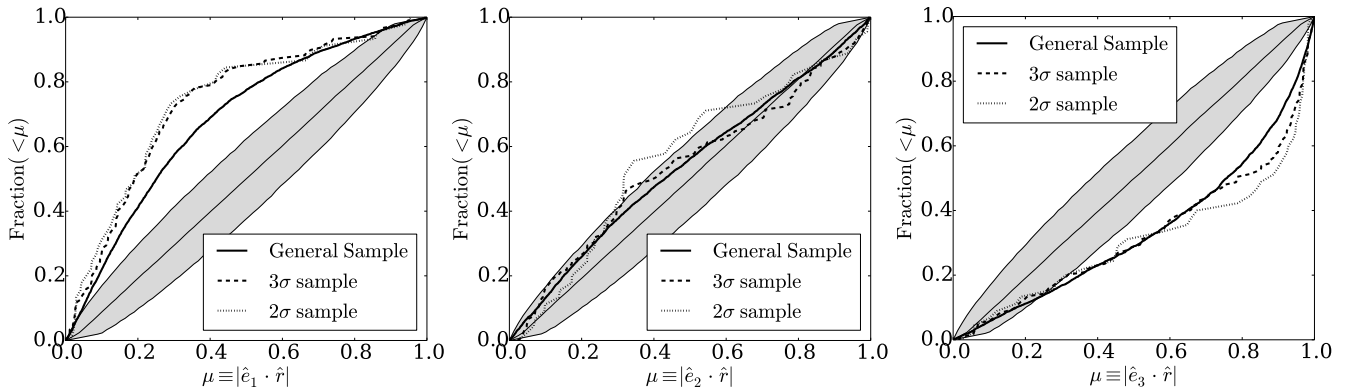

FIG. 4.— Cumulative distributions for the alignment between the vector linking the two halos in the pair, $\hat{r}$, and the three eigenvectors in the Tweb. The shaded region is the same as in Figure 3.
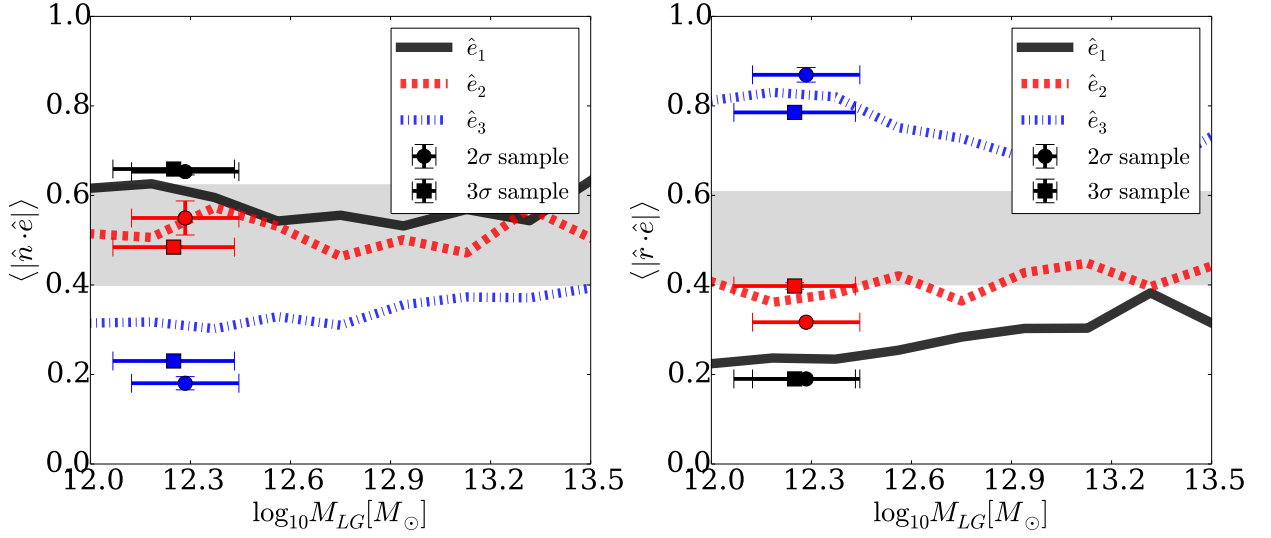
FIG. 5.— Mass dependency of the median value for the dot product between the normal/radial vector $\hat{n}/\hat{r}$ (left/right) and each one of the eigenvectors. The lines show the trends for the general sample. The error bars in the 2σ and 3σ points correspond to jackknife estimates. The shaded region shows the expectation for a random distribution without any preferential alignment, it encloses the 5% and 95% percentiles of 10000 flat distributions for μ generated with the same number of points as the 2σ sample.
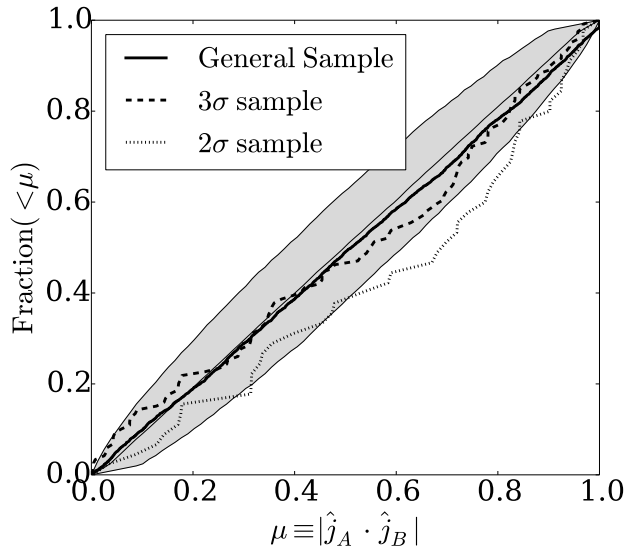
FIG. 6.— Alignment between the two angular momentum vectors of the two halos in the pair. The shaded region shows the expectation for a random distribution without a preferential alignment as it is described in Figure 5.

different samples. The straight line across the diagonal shows the expected result for vectors with randomly distributed directions.

There are two important features in Figure 3. First the alignments themselves. There is a strong anti-alignment signature between $\hat{n}$ and the third eigenvector. With respect to the first and second eigenvector the distribution is consistent with no alignment. Second, the alignment strength changes for the different samples. For the anti-alignment with $\hat{e}_3$ the signal strengthens as we move from the GS to the 3σ into the 2σ sample.

Quantitatively, the anti-alignment feature found with the $\hat{e}_3$ vector means that for 2σ sample, $\sim 50\%$ pairs have $|\mu| < 0.2$ (> 78 degrees angle), and $\sim 75\%$ pairs have $|\mu| < 0.4$ (> 66 degrees angle). These signals do not change significantly on different environments as has been already show in different alignment studies with similar (Libeskind et al. 2013) or identical (Forero-Romero et al. 2014) web finding techniques as ours. In particular, these trends hold for pairs in filaments and walls. If we consider only pairs in filaments, we have that the pair orbital angular momentum tends to be perpendicular to the filament direction, in the case of sheets it tends to lie perpendicular to the sheet plane.

The alignment strength could be explained to a great extend by a total mass dependency. In Figure 5 we show the median of $\mu \equiv \hat{e}_i \cdot \hat{n}$ and $\mu \equiv \hat{e}_i \cdot \hat{r}$ in different mass bins. Lines show the median μ-mass relation for the three eigenvectors in the GS, dots represent the results for the 2σ-3σ samples. Around the total mass $1.5 - 2.0 \times 10^{12}$ $M_\odot$ in the RS samples, the median of μ clearly from the 2σ and 3σ samples clearly differs from the GS results. However, the uncertainty level on the median for a small sample (indicated by the shaded region) makes this trend compatible with the values from the GS sample.

We also explored characteristics in the orbits which could be responsible of the strengthen alignment feature. We have that RS samples constrains the tangential velocity, as a consequence pair orbits are more eccentric as we

tighten pair constraints. For the GS sample there is no tangential velocity constraint at all. We studied the relationship between orbit eccentricity and alignment computing for each halo pair in all samples an approximate orbit eccentricity assuming a two body orbit with masses set as the virial masses and initial conditions given by current velocity vector and separation. We found that selecting a subsample of GS having the same eccentricity than 2σ-3σ samples does not increase in the alignment when compared with the full GS.

Radial Vector. Figure 4 presents the results for the eigenvectors alignments with respect to the vector connecting the two halos. In this case we find that the vector $\hat{r}$ is strongly aligned along the direction defined by $\hat{e}_3$ and anti-aligned along $\hat{e}_1$; correspondingly the signal along $\hat{e}_2$ is rather weak.

We also find a stronger signal as we move into more restrictive samples, although the signal from the GS is already very significant. Quantitatively, the alignment feature with $\hat{e}_3$ means that for the 2σ and 3σ samples, $\sim 50\%$ pairs have $|\mu| > 0.8$ (< 36 degrees angle) and $\sim 25\%$ pairs have $|\mu| > 0.95$ (< 18 degrees angle). Similar to the previous case of the $\hat{n}$ vector, the increasing strength of the $\hat{r}$ alignment can be explained to a great extent by a selection on mass.

Considering that the 2σ and 3σ samples correspond to pairs moving along the radial direction, we can say that the motion of the LG halos is mostly done along the $\hat{e}_3$ vectors. This is consistent with recent results that report a strong alignment of halo's peculiar velocities along that direction (Forero-Romero et al. 2014).

Halo Spin. We also explore the alignment of the angular momentum (spin) of each pair member $\hat{j}_A$ and $\hat{j}_B$ with each other, the orbital angular momentum and with the cosmic web.

Figure 6 shows the cumulative distribution of dot product between angular momentum of the two halos. We find a a slight alignment of spin vectors for the 2σ sample with a median around $|\mu| \sim 0.7$ (45 degrees) which is barely above the no-alignment expectation marked by the shaded region. Furthermore, we found no significant alignment with the pair orbital angular momentum nor the cosmic web.

The absence of alignment for the spins is consistent with different studies of spin alingment that mark the range $10^{12} M_\odot$ as either a transition mass from alignment into anti-alignment or from no-alignment into alignment (Hahn et al. 2007; Aragón-Calvo et al. 2007; Zhang et al. 2009; Codis et al. 2012; Trowland et al. 2013; Libeskind et al. 2013; Forero-Romero et al. 2014). We refer the reader to Table 2 in Forero-Romero et al. (2014) for a review on the different results of spin alignment with the cosmic web in cosmological simulations. It seems that this transition has to do with the changes on the major merger rate as a dark matter halo approaches the $10^{12} M_\odot$ mass (Forero-Romero 2009; Codis et al. 2012).

In the LG, the angle between MW and M31 spin is $\sim 60°$ ($|\mu| = 0.5$) and the angles between spins and orbital angular momentum are $\sim 33°$ ($|\mu| = 0.83$) and $\sim 76°$ ($|\mu| = 0.24$) for MW and M31 respectively (van der Marel et al. 2012a). This is consistent with our results of no strong alignment.

5. DISCUSSION AND CONCLUSIONS

The mass range of the LG pairs is tightly correlated with the properties of the web in which they reside, as shown in Table 1 and Figure 1. This confirms that the local overdensity, the trace of the tidal tensor, is the dominant web parameter that define the abundance and properties of halos (Lee & Shandarin 1998; Lemson & Kauffmann 1999; Sheth & Tormen 2004; Fakhouri & Ma 2009; Alonso et al. 2014). Other quantities derived from the tidal tensor play a secondary role defining properties such as its formation history.

In our case, the fact that the preferred LG total mass is around $1 - 4 \times 10^{12} M_\odot$ implies that the preferred environment are filaments and sheets with an overdensity close to the average value. Correspondingly, the values for the ellipticity and prolateness are also well defined for the LG pairs given its correlation with the total mass.

We conclude that the typical LG environment and its characteristics is a robust results depending mostly on the LG total mass.

The alignments with the cosmic web have also a mass dependency. Although they seem to be stronger once the kinematic constraints are imposed on the GS pairs, the results are consistent with the a simple mass cut on the GS sample. There is a clear anti-alignment between the third eigenvector and the orbital angular momentum vector, meaning that this vector is perpendicular to filaments and the sheets, We also found that the vector joining the LG halos are aligned with the third eigenvector. This means that he pair is aligned with the filaments and lies on the sheets and its motion is done along these directions.

These alignment features are in agreement with the scenario that pairs created in-situ or falling into a filament/wall align their orbits with the large scale structure in a relaxation process where pair members tend to moves along the slowest collapsing directions.

How can we relate these alignments to the observed LG? To evaluate this point we use observational information for the satellite distribution around the LG galaxies. The MW satellites are located at high galactic latitudes forming a planar structure that forms an angle of $42° - 52°$ ($\mu = 0.6 - 0.7$) with the vector joining the MW and M31; while the M31 satellites are on a plane that lies on the same vector (Pawlowski et al. 2013; Shaya & Tully 2013).

Most ΛCDM studies find that sub-structure infall direction is done along $\hat{e}_3$ (the direction of filaments) (Zentner et al. 2005; Bailin et al. 2008) or almost over the plane defined by the $\hat{e}_2$ and $\hat{e}_3$ (Libeskind et al. 2014).

Taking this three points together (the alignment of MW-M31 along $\hat{e}_3$, the observed satellite alignments and the preferential infall along $\hat{e}_3$) we have that the M31 plane of satellites is completely consistent with the average alignment picture we have described. However, the plane defined by the MW satellites should also be close to parallel with respect to the vector joining MW and M31 and the plane of M31 satellites. Instead, this plane has $\mu = 0.6 - 0.7$ with respect to these directions. Therefore, we suggest that the spatial location of MW satellites raises a potential contradiction with the average expectations from ΛCDM, a point that has been mentioned before (Pawlowski et al. 2012, 2014).

This apparent contradiction can be solved if one considers that the subhalo infall properties depend on the environment at *the merger time*, while the alignments for yet unvirialized pairs such as the dominant galaxis in the LG depend on the current state of the cosmic web. This also explain the absence of a strong alignment with halo spin, because it reflects past configurations of the web, not the current one. From this perspective, a joint consideration of the alignments between the dominant halos in the LG and their satellites, which also feature strong signals (Kroupa et al. 2005; Pawlowski et al. 2013; Shaya & Tully 2013), should inform us about the structural evolution of the cosmic web around the LG.

Our results raise the need to observationally constrain the alignments of LG pairs with their cosmic web environment. To this end one could use mass reconstructions from large surveys (Wang et al. 2009; Muñoz-Cuartas et al. 2011; Nuza et al. 2014; Wang et al. 2014) or filament finders (González & Padilla 2010; Sousbie 2011) to select a LG sample to quantify the alignments with the surrounding filamentary structure. This would allow not only a direct quantification of how common are the LG alignments but also provide a new test of ΛCDM.

REFERENCES

Alonso, D., Eardley, E., & Peacock, J. A. 2014, ArXiv e-prints
Aragon-Calvo, M. A., Silk, J., & Szalay, A. S. 2011, MNRAS, 415, L16
Aragón-Calvo, M. A., van de Weygaert, R., Jones, B. J. T., & van der Hulst, J. M. 2007, ApJ, 655, L5
Bailin, J., Power, C., Norberg, P., Zaritsky, D., & Gibson, B. K. 2008, MNRAS, 390, 1133
Cautun, M., van de Weygaert, R., Jones, B. J. T., & Frenk, C. S. 2014, MNRAS, 441, 2923
Codis, S., Pichon, C., Devriendt, J., Slyz, A., Pogosyan, D., Dubois, Y., & Sousbie, T. 2012, MNRAS, 427, 3320
Courtois, H. M., Pomarède, D., Tully, R. B., Hoffman, Y., & Courtois, D. 2013, AJ, 146, 69
Cox, T. J., & Loeb, A. 2008, MNRAS, 386, 461
Fakhouri, O., & Ma, C.-P. 2009, MNRAS, 394, 1825
Forero-Romero, J. E. 2009, MNRAS, 399, 762
Forero-Romero, J. E., Contreras, S., & Padilla, N. 2014, MNRAS, 443, 1090
Forero-Romero, J. E., Hoffman, Y., Bustamante, S., Gottlöber, S., & Yepes, G. 2013, ApJ, 767, L5
Forero-Romero, J. E., Hoffman, Y., Gottlöber, S., Klypin, A., & Yepes, G. 2009, MNRAS, 396, 1815

Forero-Romero, J. E., Hoffman, Y., Yepes, G., Gottlöber, S., Piontek, R., Klypin, A., & Steinmetz, M. 2011, MNRAS, 417, 1434

González, R. E., Kravtsov, A. V., & Gnedin, N. Y. 2013, ApJ, 770, 96

—. 2014, ApJ, 793, 91

González, R. E., & Padilla, N. D. 2010, MNRAS, 407, 1449

Hahn, O., Carollo, C. M., Porciani, C., & Dekel, A. 2007, MNRAS, 381, 41

Hinshaw, G., Larson, D., Komatsu, E., Spergel, D. N., Bennett, C. L., Dunkley, J., Nolta, M. R., Halpern, M., Hill, R. S., Odegard, N., Page, L., Smith, K. M., Weiland, J. L., Gold, B., Jarosik, N., Kogut, A., Limon, M., Meyer, S. S., Tucker, G. S., Wollack, E., & Wright, E. L. 2013, ApJS, 208, 19

Karachentsev, I. D. 2005, AJ, 129, 178

Klypin, A., Hoffman, Y., Kravtsov, A. V., & Gottlöber, S. 2003, ApJ, 596, 19

Klypin, A., & Holtzman, J. 1997, ArXiv Astrophysics e-prints

Klypin, A. A., Trujillo-Gomez, S., & Primack, J. 2011, ApJ, 740, 102

Kroupa, P., Theis, C., & Boily, C. M. 2005, A&A, 431, 517

Lee, J., & Shandarin, S. F. 1998, ApJ, 500, 14

Lemson, G., & Kauffmann, G. 1999, MNRAS, 302, 111

Li, Y.-S., & White, S. D. M. 2008, MNRAS, 384, 1459

Libeskind, N. I., Hoffman, Y., Forero-Romero, J., Gottlöber, S., Knebe, A., Steinmetz, M., & Klypin, A. 2013, MNRAS, 428, 2489

Libeskind, N. I., Knebe, A., Hoffman, Y., & Gottlöber, S. 2014, MNRAS, 443, 1274

Mei, S., Blakeslee, J. P., Côté, P., Tonry, J. L., West, M. J., Ferrarese, L., Jordán, A., Peng, E. W., Anthony, A., & Merritt, D. 2007, ApJ, 655, 144

Muñoz-Cuartas, J. C., Müller, V., & Forero-Romero, J. E. 2011, MNRAS, 417, 1303

Nuza, S. E., Kitaura, F.-S., Heß, S., Libeskind, N. I., & Müller, V. 2014, MNRAS, 445, 988

Pawlowski, M. S., Famaey, B., Jerjen, H., Merritt, D., Kroupa, P., Dabringhausen, J., Lüghausen, F., Forbes, D. A., Hensler, G., Hammer, F., Puech, M., Fouquet, S., Flores, H., & Yang, Y. 2014, MNRAS, 442, 2362

Pawlowski, M. S., Kroupa, P., Angus, G., de Boer, K. S., Famaey, B., & Hensler, G. 2012, MNRAS, 424, 80

Pawlowski, M. S., Kroupa, P., & Jerjen, H. 2013, MNRAS, 435, 1928

Riebe, K., Partl, A. M., Enke, H., Forero-Romero, J., Gottlöber, S., Klypin, A., Lemson, G., Prada, F., Primack, J. R., Steinmetz, M., & Turchaninov, V. 2013, Astronomische Nachrichten, 334, 691

Sandage, A., & Tammann, G. A. 1975, ApJ, 196, 313

Shaya, E. J., & Tully, R. B. 2013, MNRAS, 436, 2096

Sheth, R. K., & Tormen, G. 2004, MNRAS, 350, 1385

Sohn, S. T., Anderson, J., & van der Marel, R. P. 2012, ApJ, 753, 7

Sousbie, T. 2011, MNRAS, 414, 350

Trowland, H. E., Lewis, G. F., & Bland-Hawthorn, J. 2013, ApJ, 762, 72

van der Marel, R. P., Besla, G., Cox, T. J., Sohn, S. T., & Anderson, J. 2012a, ApJ, 753, 9

van der Marel, R. P., Fardal, M., Besla, G., Beaton, R. L., Sohn, S. T., Anderson, J., Brown, T., & Guhathakurta, P. 2012b, ApJ, 753, 8

Wang, H., Mo, H. J., Jing, Y. P., Guo, Y., van den Bosch, F. C., & Yang, X. 2009, MNRAS, 394, 398

Wang, H., Mo, H. J., Yang, X., Jing, Y. P., & Lin, W. P. 2014, ApJ, 794, 94

Zentner, A. R., Kravtsov, A. V., Gnedin, O. Y., & Klypin, A. A. 2005, ApJ, 629, 219

Zhang, Y., Yang, X., Faltenbacher, A., Springel, V., Lin, W., & Wang, H. 2009, ApJ, 706, 747